ADVANCED ENERGY MATERIALS
www.advenergymat.de

Understanding and Minimizing V_{OC} Losses in All-Perovskite Tandem Photovoltaics

Jarla Thiesbrummel, Francisco Peña-Camargo, Kai Oliver Brinkmann, Emilio Gutierrez-Partida, Fengjiu Yang, Jonathan Warby, Steve Albrecht, Dieter Neher, Thomas Riedl, Henry J. Snaith,* Martin Stolterfoht,* and Felix Lang**

Understanding performance losses in all-perovskite tandem photovoltaics is crucial to accelerate advancements toward commercialization, especially since these tandem devices generally underperform in comparison to what is expected from isolated layers and single junction devices. Here, the individual sub-cells in all-perovskite tandem stacks are selectively characterized to disentangle the various losses. It is found that non-radiative losses in the high-gap subcell dominate the overall recombination in the baseline system, as well as in the majority of literature reports. Through a multi-faceted approach, the open-circuit voltage (V_{OC}) of the high-gap perovskite subcell is enhanced by 120 mV. Employing a novel (quasi) lossless indium oxide interconnect, this enables all-perovskite tandem solar cells with 2.00 V V_{OC} and 23.7% stabilized efficiency. Reducing transport losses as well as imperfect energy-alignments boosts efficiencies to 25.2% and 27.0% as identified via subcell selective electro- and photo-luminescence. Finally, it is shown how, having improved the V_{OC}, improving the current density of the low-gap absorber pushes efficiencies even further, reaching 25.9% efficiency stabilized, with an ultimate potential of 30.0% considering the bulk quality of both absorbers measured using photo-luminescence. These insights not only show an optimization example but also a generalizable evidence-based optimization strategy utilizing optoelectronic sub-cell characterization.

1. Introduction

With the discovery that mixed-metal halide perovskites enable much lower bandgaps than their neat-lead or neat-tin based counterparts, significant efforts commenced on the development of all-perovskite tandem solar cells.[1–5] Combining low-bandgap (LG) and high-bandgap (HG) perovskites in tandem solar cells overcomes the fundamental efficiency limits of their single junction counterparts, without the need for combining with more traditional low-bandgap materials used previously such as Si or copper indium gallium selenide.[6–10] All-perovskite tandems promise highest efficiencies, on par with perovskite/silicon tandem technologies, while using much thinner absorber layers, and move away from the energy intensive production of crystalline silicon. They can also be much lighter, which makes them a promising option for a range of different applications: from building- or vehicle-integrated photovoltaics (PV) to high-altitude and

J. Thiesbrummel, F. Peña-Camargo, E. Gutierrez-Partida, J. Warby, D. Neher, M. Stolterfoht, F. Lang
Institute of Physics and Astronomy
University of Potsdam
Karl-Liebknecht-Str. 24–25, 14476 Potsdam-Golm, Germany
E-mail: jarla.thiesbrummel@physics.ox.ac.uk; stolterf@uni-potsdam.de; lang1@uni-potsdam.de

J. Thiesbrummel, H. J. Snaith
Clarendon Laboratory
University of Oxford
Parks Road, Oxford OX1 3PU, UK
E-mail: henry.snaith@physics.ox.ac.uk

The ORCID identification number(s) for the author(s) of this article can be found under https://doi.org/10.1002/aenm.202202674.

© 2022 The Authors. Advanced Energy Materials published by Wiley-VCH GmbH. This is an open access article under the terms of the Creative Commons Attribution License, which permits use, distribution and reproduction in any medium, provided the original work is properly cited.

DOI: 10.1002/aenm.202202674

K. O. Brinkmann, T. Riedl
Institute of Electronic Devices and Wuppertal Center for Smart Materials & Systems
University of Wuppertal
Rainer-Gruenter-Str. 21, 42119 Wuppertal, Germany

F. Yang, S. Albrecht
Young Investigator Group Perovskite Tandem Solar Cells
Helmholtz-Zentrum Berlin für Materialien und Energie GmbH
Kekuléstraße 5, 12489 Berlin, Germany

S. Albrecht
Technical University Berlin
Faculty IV – Electrical Engineering and Computer Science
Marchstr. 23, 10587 Berlin, Germany

 © 2022 The Authors. Advanced Energy Materials published by Wiley-VCH GmbH

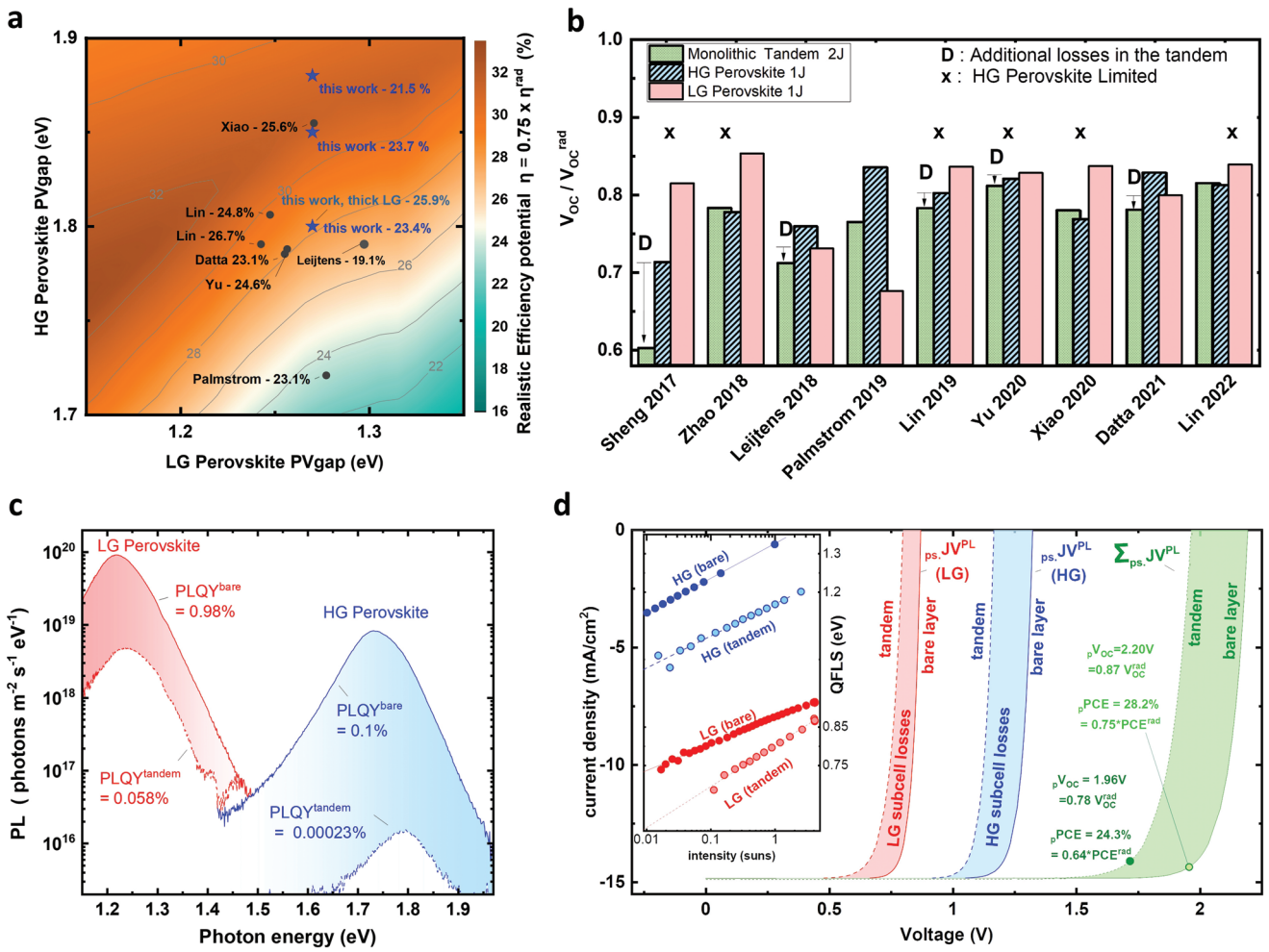

Figure 1. a) Literature overview of various all-perovskite tandem solar cells indicating the achieved efficiency, plotted as a function of the employed high-and low-bandgap perovskites. For consistency, we determined the individual bandgaps from reported external quantum efficiencies (EQE), via d(EQE)/dE, and denoted this as PVgap. The color map displays the realistic efficiency potential for specific bandgap combinations (defined as 75% of the radiative efficiency limit). b) Relative V_{OC} losses in monolithic all-perovskite tandems from (a), as well as the corresponding high-gap and low-gap single junction devices.[13,16,17,26–32] c) Photoluminescence (PL) of high- and low-gap perovskites fabricated individually on glass (isolated bare layers) and incorporated in a monolithic tandem. d) Pseudo-*JV* curves reconstructed from intensity-dependent PL measurements highlighting V_{OC} losses.

even space PV where they also benefit from their radiation hardness.[11] Their energy-efficient processability, either from solution or by thermal evaporation at ambient temperatures, is roll-to-roll compatible and could allow a much more cost-efficient technology with shorter energy payback times compared to current technologies, or even perovskite/Si tandem PV.[12]

The solar to electrical power conversion efficiency (PCE) for 2-Terminal all-perovskite tandems has increased from 17% for the first attempts, to the current record of 26.4%.[3,13,14] We give an overview of this rapid progress in **Figure 1**a, by plotting the employed bandgap combinations and the achieved power conversion efficiencies, alongside a realistic efficiency potential of $\approx 0.75 \times PCE^{rad}$. Here PCE^{rad} is the radiative efficiency from the detailed balance limit assuming a step function absorption profile for each band gap (see Supporting Information for calculation details). A large focus has been on improving the efficiency and stability of the low-bandgap lead-tin perovskite.[5,13,15–17] However, as we illustrate in Figure 1b, the high-gap perovskites dominate the open-circuit voltage (V_{OC}) losses for most tandem devices, especially after significant improvement of low bandgap perovskites over the past 3 years. Overcoming the V_{OC} losses in the high-gap perovskite subcell, which typically increase for higher bandgap perovskites,[18–20] therefore offers room for further improvements. Moreover, the incorporation of the high-gap and low-gap perovskites in a tandem often leads to significant additional V_{OC} penalties. This can be due to degradation of the underlying subcell or layers during subsequent layer deposition, be it via sputtering or from solution, additional interfacial recombination induced by the interconnecting layer, or processing issues and inhomogeneities. We highlight several of those cases with a "D" in Figure 1b.

To understand where these losses come from and how they can be reduced, it is important to not just look at the overall tandem performance and single junction cells, but characterize the behavior of both subcells when incorporated in the complete tandem device. Traditional electrical characterization of the monolithic tandem, however, provides little information on the behavior of the individual subcells. Current-voltage

© 2022 The Authors. Advanced Energy Materials published by Wiley-VCH GmbH

JV-measurements performed on corresponding single junction devices that are often reported alongside tandem results and used in Figure 1b, do not necessarily reflect subcell performance once integrated in the tandem accurately. Quantitative measurements that provide information on the different subcells within the monolithic tandem stack individually are therefore crucial to understand performance-limiting layers and mechanisms. Electro- and photo-luminescence (EL & PL) can be measured from each sub-cell selectively in monolithic interconnected tandem devices. These techniques have previously been employed by the III/V solar cell community to investigate subcell performance in multijunction solar cells.[21–24] We recently extended these approaches to reveal efficiency limits in perovskite/silicon tandems.[25] However, although 2-terminal all perovskite tandem cells have become a topic of great interest, and subcell selective characterization can provide valuable insights to accelerate development, such an extensive subcell selective characterization has to date never been carried out for these systems.

Herein, we conduct extensive PL and EL characterization of isolated perovskite films, single junction devices, and complete all-perovskite tandem cells, in order to identify the factors limiting the performance in these cells in comparison with the thermodynamic efficiency limit. We reveal that the high-band gap sub cell is predominantly responsible for the V_{OC} losses in our own complete tandem devices, as well as in many tandem devices from literature at the moment. We employ a threefold optimization strategy for the high-band gap perovskite, consisting of; i) addition of oleylamine to the perovskite in combination with, ii) a lithium fluoride (LiF) layer between the perovskite and the electron transport layer (ETL) and, iii) the use of the self-assembled monolayer (SAM) 2PACz instead of the frequently used hole transport layer (HTL) poly[bis(4-phenyl)(2,4,6-trimethylphenyl)amine (PTAA). We apply our threefold optimization approach to triple cation-based high-gap perovskites with bandgaps ranging from 1.80 through 1.85 to 1.88 eV and find a robust reduction of V_{OC} losses for all tested bandgaps. This is important since the latter two bandgaps promise highest power conversion efficiencies in combination with the 1.27 eV perovskite used herein (Figure 1b). We thereafter use the optimized high-gap perovskites to fabricate efficient all-perovskite tandem solar cells, reaching steady-state efficiencies of up to 23.4%, 23.7%, and 21.5% for 1.80 eV/1.27 eV, 1.85 eV/1.27 eV and 1.88 eV/1.27 eV bandgap combinations, respectively. Coming back to the subcell characterization, we then characterize these optimized all-perovskite tandems, and are able to determine the efficiency potential that could be achieved if transport losses and energy-level mismatches in the stack were eliminated. Furthermore, we also show that the interconnect we employed is lossless. Overall, our versatile sub-cell characterization approach will facilitate evidence-based optimization of future all-perovskite tandem cells.

2. Results

2.1. Assessing the Limiting Junction in the Tandem Cells

In order to investigate whether the V_{OC} losses in our all-perovskite tandems are dominated by the high- or the low-gap perovskite subcells, we measured the photoluminescence quantum yield (PLQY) selectively by excitation with 520 and 818 nm in a monolithic all perovskite tandem (based on a 1.27 eV low-gap and 1.80 eV high-gap combination with an efficiency of 20.9% under AM1.5G) and compared it to the PLQY of identically prepared isolated high-gap (PLQY = 0.1%) and low-gap (PLQY = 0.98%) perovskite layers on glass (Figure 1c). Interestingly, the PLQY of the high-gap perovskite is reduced by three orders of magnitude in the tandem device, compared to the isolated layer, whereas the low-gap perovskite is only reduced ≈20-fold. Since the quasi-Fermi level splitting (QFLS) is directly given by the PLQY and the radiative limit of the semiconducting material ($QFLS_{rad}$, see Supporting Information) via Equation (1), we conclude that the high-gap perovskite strongly dominates V_{OC} losses also in our system.

$$QFLS = QFLS_{rad} + k_B T \cdot \ln(PLQY) \tag{1}$$

To further understand the potential of our tandem with the given absorbers, we now measure intensity-dependent photoluminescence yields (iPLQY) which allows us to determine a QFLS at each intensity. We then construct "pseudo-JV curves" by plotting the total recombination current at each excitation intensity minus the generation current (J_{SC}) on the y–axis versus the QFLS on the x–axis (Figure 1d). Comparison of pseudo-JV curves derived from iPLQY measurements on isolated films versus measurements in the monolithic tandem stack exemplifies V_{OC} losses present in the tandem configuration. It also shows that these losses are dominated by the high-gap perovskite. Summing the QFLS obtained for the high-gap and low-gap perovskite isolated layers and subcells further allows us to construct pseudo-JV curves of corresponding tandems that are free of resistive losses and, in case of the isolated layers, additionally free of interface recombination from the various contact layers, processing damage, etc. This efficiency potential constructed from isolated layer measurements reaches 28.2%, a value that corresponds to the practical efficiency potential of around 0.75 × PCE^{rad}. We present a more detailed analysis as well as strategies to reach this potential at the end of this work.

2.2. Minimization of V_{OC} Losses in HG Perovskites

To understand the origins of V_{OC} limitations in our high-gap perovskite we measured the PLQY of 1.80 eV bandgap triple-cation based perovskites ($Cs_{0.05}(FA_{0.60}MA_{0.40})_{0.95}Pb(I_{0.60}Br_{0.40})_3$) with and without the hole-and electron transport layers (HTL and ETL respectively). Comparing the PLQY of a perovskite layer prepared on glass and on PTAA, our standard HTL, as displayed in **Figure 2**a, reveals that the PTAA is strongly limiting the PLQY. This limitation is known and has been addressed in the past by using self-assembled monolayer (SAM) HTLs instead of conventional HTLs.[33,34] Their use as a hole selective contact can strongly reduce non-radiative losses at the perovskite—HTL interface compared to the conventionally used PTAA,[33] which is particularly a problem for wide-gap perovskites (>1.75 eV).[19]

Changing the HTL from PTAA to 2PACz significantly improves the PLQY of our 1.80 eV triple-cation based perovskites (Figure 2a), indicating a reduction of interfacial recombination at the HTL side, which was strongly limiting before. Having

© 2022 The Authors. Advanced Energy Materials published by Wiley-VCH GmbH

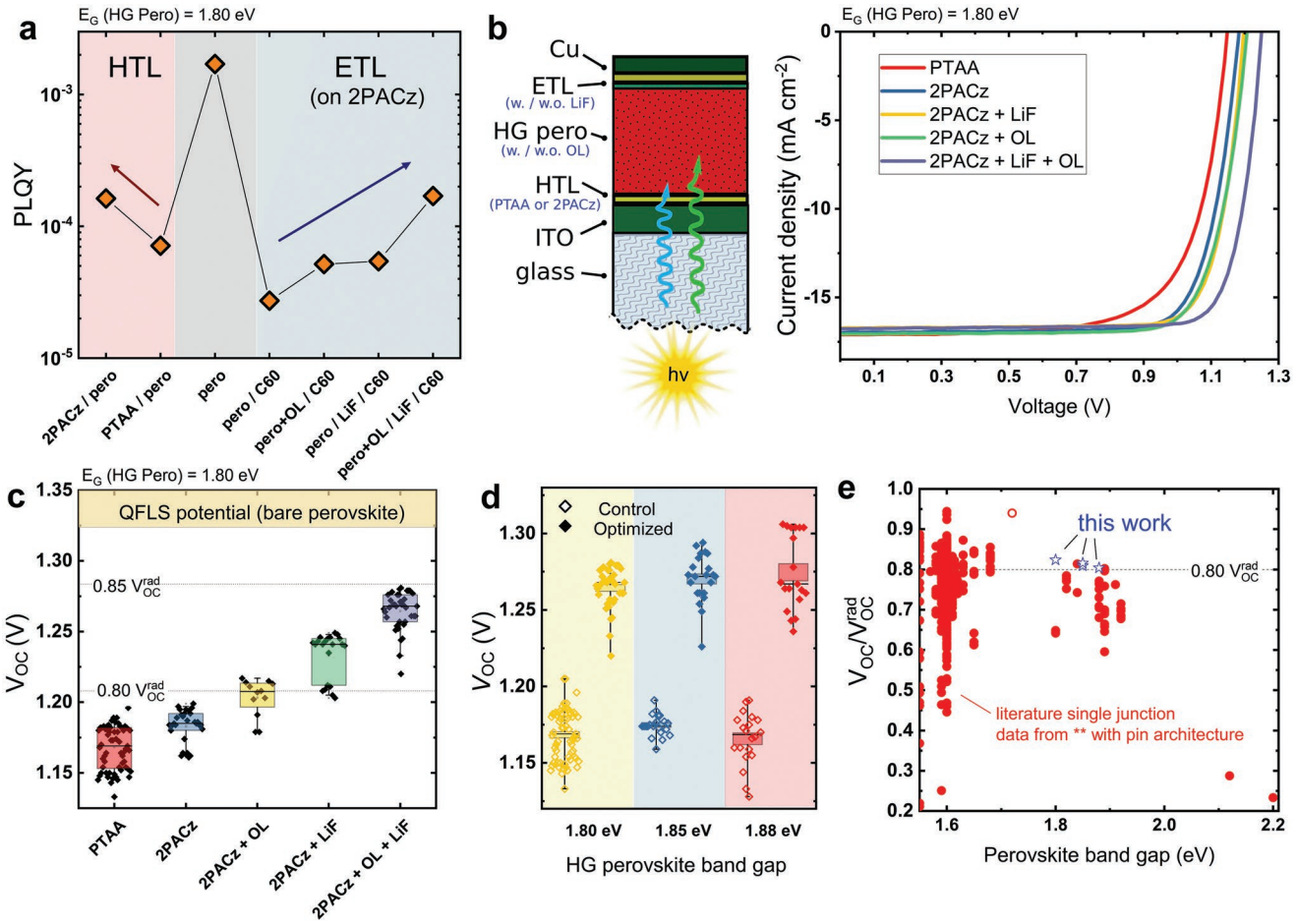

Figure 2. a) PLQY measured on different partial stacks. b) Schematic overview of the HG single junction solar cell and *JV* curves for 1.80 eV $Cs_{0.05}(FA_{0.60}MA_{0.40})_{0.95}Pb(I_{0.60}Br_{0.40})_3$ perovskite solar cells for various optimization steps. c) The V_{OC} from the solar cells in (b), plotted as a function of the different optimization steps. The dashed line displays the radiative V_{OC} limit (V_{OC}^{rad}), which is 1.51 V for perovskites with a 1.80 eV bandgap. d) V_{OC} statistics for optimized and control HG perovskite solar cells with bandgaps of 1.80, 1.85, and 1.88 eV. e) The V_{OC} divided by the radiative V_{OC} limit for recent pin perovskites with a range of different bandgaps, extracted from The Perovskite Database.[20] The open circle indicates a device with an ETL based on an alternative fullerene blend.[40] The stars indicate our work and show optimized (champion) solar cells based on perovskites bandgaps at 1.80, 1.85, and 1.88 eV.

removed the dominating HTL-Pero-interface limitation now allows us to address the perovskite-ETL interface. We first try inserting a thin layer of LiF between the perovskite and the ETL, forming a strong surface dipole that repels minority carriers away from the interface, thereby reducing interfacial recombination.[34–36] In order to reduce the recombination losses further, we then added oleylamine into the perovskite precursor solution, which has previously been shown to improve the efficiency of lead-based perovskite solar cells through both grain- and interface modifications.[37] Interestingly when we tested a combined approach of adding oleylamine to the perovskite precursor and inserting a thin LiF layer we found that they worked in an additive fashion, increasing the QFLS to exactly the sum of the individual improvements (Figure 2a).

We subsequently fabricated single junction solar cells with the structure glass/ITO/PTAA or 2PACz/1.80 eV bandgap triple-cation based perovskite w/ or w/o oleylamine and w/ or w/o LiF/ETL/Cu to test our threefold optimization approach prior to its incorporation into tandem devices. Looking at the *JV* curves displayed in Figure 2b, it can be seen that the improvement in PLQY directly translates into an increased V_{OC} in devices. As seen in **Table 1**, summarizing device parameters and statistics (more statistics can be found in Figure S1, Supporting Information), the V_{OC} improves ≈90 mV for the fully optimized device compared to control devices, which equals the sum of the individual gains. Figure 2c shows that every step of our threefold optimization brings the V_{OC} significantly closer toward the limit imposed by the bulk quality of the perovskite absorber, which is 1.32 V as determined from PLQY measurements of isolated perovskite absorbers. Notably, the threefold optimized devices reach an average V_{OC} of 1.26 V (max 1.29 V) which is around 83% of the radiative V_{OC} limit of 1.51 V for devices with a 1.80 eV bandgap. Ultimately, we tested the long-term stability of our threefold passivation approach step by step by tracking the efficiency under AM1.5G or equivalent illumination conditions and found that fully passivated devices outperform control devices, see Figures S21 and S22, Supporting Information.

© 2022 The Authors. Advanced Energy Materials published by Wiley-VCH GmbH

Table 1. Device parameters and statistics for the different optimized and control single junction devices using a 1.80 eV HG perovskite absorber. ΔV_{OC} and ΔFF indicate the improvement in these respective values compared to the unoptimized control device on PTAA.

	V_{OC} [V]	J_{SC} [mA cm^{-2}]	FF [%]	PCE [%]	ΔV_{OC} [mV]	ΔFF [%]
PTAA device	1.17 ± 0.02	17.0 ± 0.5	75.6 ± 2.9	15.0 ± 1.0	–	–
2PACz device	1.18 ± 0.01	17.2 ± 0.7	78.8 ± 1.4	16.1 ± 0.6	10	3.2
2PACz + OAm	1.20 ± 0.01	17.1 ± 0.2	77.2 ± 2.0	15.9 ± 0.7	30	1.6
2PACz + LiF	1.23 ± 0.02	17.1 ± 0.5	78.9 ± 2.0	16.6 ± 0.6	60	3.3
2PACZ + OAm and LiF	1.26 ± 0.01	16.6 ± 0.5	79.1 ± 2.0	16.6 ± 0.6	90	3.5

We tested the robustness of this threefold optimization route with various high-bandgap perovskite compositions by varying the Br-ratio from the initial 0.4 to 0.45 and 0.5. This allowed us to vary the perovskite bandgap from 1.80 eV to 1.85 and 1.88 eV respectively, as determined from EQE. Control devices based on the 1.85 and 1.88 eV perovskites both reached 1.17 V V_{OC} on average, see Figure S2, Supporting Information. Using our threefold optimization significantly improved the V_{OC} to 1.27 V and 1.28 V, thereby achieving remarkable V_{OC}/V_{OC}^{rad} ratios of 0.82 and 0.81, respectively, as can be seen in Figure 2d. This improvement becomes even more apparent when comparing our achieved V_{OC} with data obtained from literature. In Figure 2e we display the ratio of the V_{OC} divided by the V_{OC}^{rad} as a function of the perovskite bandgap for a large number of perovskite pin devices, extracted from The Perovskite Database.[20] Clearly visible is a general trend of decreasing V_{OC}/V_{OC}^{rad} with increasing bandgap.[38] This effect has been assigned to different phenomena, from halide segregation (or Hoke effect), to interface recombination, improper energy alignment, or high defect densities at the surface of the perovskite.[18,19,39] There is also evidence to suggest that the use of C_{60} as an ETL is the cause of the limited V_{OC}s, with other fullerenes (or fullerene blends) showing promise to overcome these issues (open circle in Figure 2e).[40]

Our optimized 1.80, 1.85, and 1.88 eV perovskite based single junction devices (blue stars) thereby reach comparatively high V_{OC}/V_{OC}^{rad} ratios, well above 0.8. This highlights that our threefold optimization route that was initially developed for the HG perovskite with a bandgap of 1.80 eV, is applicable to a wider range of perovskite compositions. A robust passivation strategy is critical for future all-perovskite tandem development to unlock highest efficiencies with optimal HG – LG bandgap combinations, as shown in Figure 1a.

2.3. Implementation in Tandems

In a next step, we integrated our threefold optimized high-gap perovskites into monolithic all perovskite tandems. For this purpose, we use a 1.27 eV (as determined by d(EQE)/dE) low-gap $FA_{0.83}Cs_{0.17}Pb_{0.5}Sn_{0.5}I_3$ perovskite subcell, which we deposited on top of the high-gap subcells. The complete layer stack comprises glass/ITO/PTAA or 2PACz/HG-Perovskite/C_{60}/AZO-nanoparticles/ALD-SnO_x/ALD-InO_x/PEDOT:PSS/LG-Perovskite/C_{60}/BCP/copper as shown in **Figure 3**a alongside a cross-sectional scanning electron microscopy image of the all-perovskite tandem structure. Our recombination layer comprises an ultrathin (≈1.5 nm) layer of indium oxide, like we have reported previously for perovskite/organic tandem

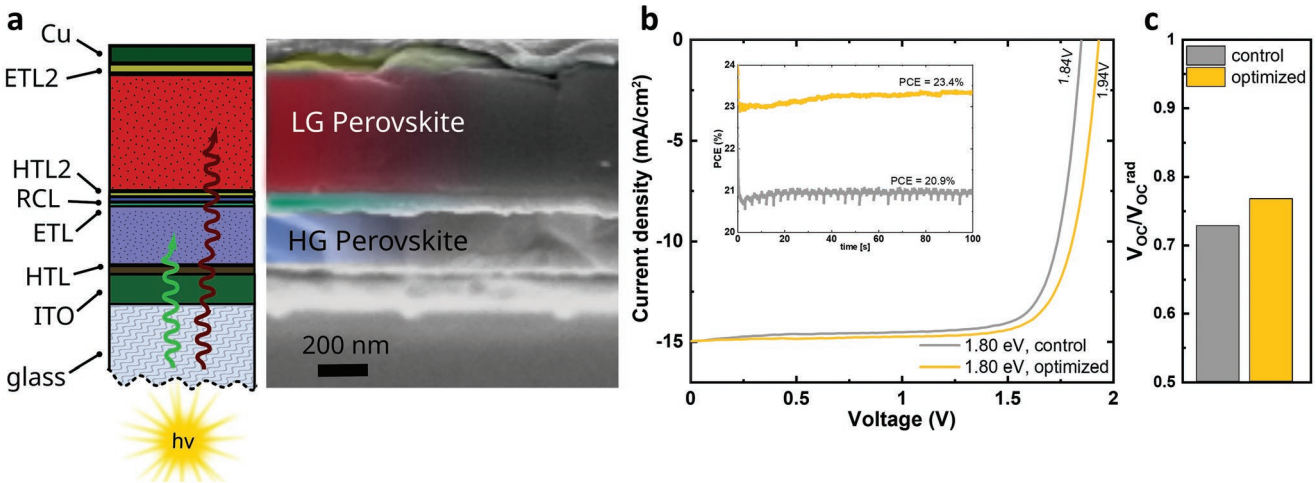

Figure 3. a) Schematic overview of the all-perovskite tandem structure alongside a cross-sectional scanning electron microscopy (SEM) image of an all-perovskite tandem with optimized HG perovskite. b) *JV* curves of a tandem with optimized 1.80 eV HG perovskite subcell, and a control tandem. In the inset, MMP tracking is displayed for both of these devices. The optimized wide-gap cell directly translates into improved tandem cell devices with efficiencies reaching over 23%. c) V_{OC}/V_{OC}^{rad} ratios for the control and optimized tandems displayed in (b).

© 2022 The Authors. Advanced Energy Materials published by Wiley-VCH GmbH

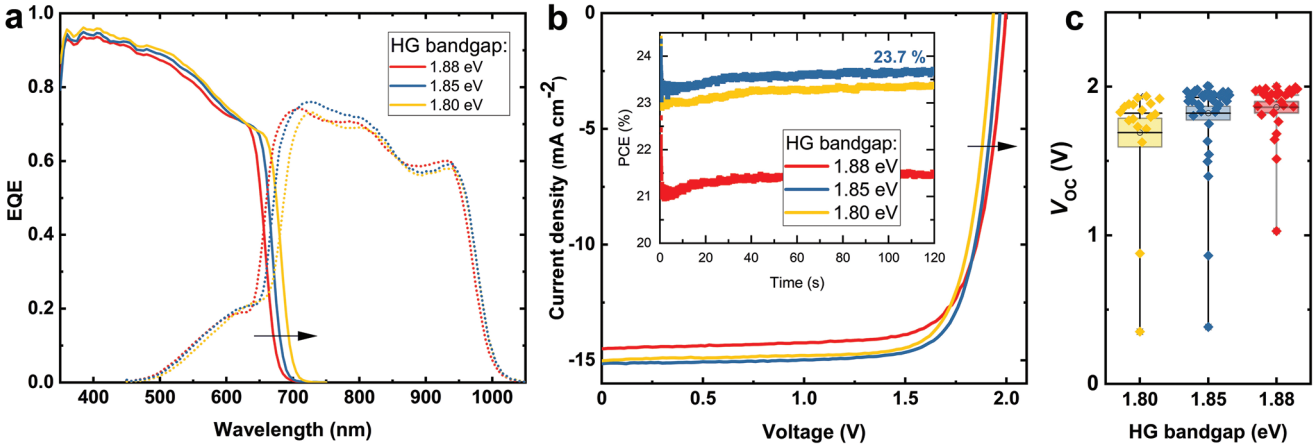

Figure 4. a) EQE spectra for all-perovskite tandems fabricated using three different HG perovskite bandgaps. These spectra alongside the integrated J_{SC} values are shown in Figure S3, Supporting Information. We note that the high EQE at low wavelengths can be explained by light incoupling from ITO due to the high refractive index of the perovskite absorber material.[44] b) *JV* curves for representative tandems with three different HG perovskite bandgaps. Best performing MPP tracking is displayed in the inset. c) Statistical overview of the V_{OC} for the different tandem systems. Further device statistics can be found in Figure S4, Supporting Information.

solar cells.[41] This indium oxide layer is deposited by atomic layer deposition (ALD) on top of a hybrid AZO-NP/ALD SnO_x layer that functions as internal barrier layer, stabilizing and protecting the layers underneath from follow up processing.[42,43] This is the first time that such an interconnect is implemented in a perovskite/perovskite tandem structure.

As seen in the *JV* characteristics in Figure 3b, our all-perovskite tandems with optimized HG perovskite sub-cells reach a much higher V_{OC}, than the non-optimized control tandems. The improvement in V_{OC}, of ≈120 mV, is consistent with the improvement observed in the optimized HG single junctions, and we present more detailed sub-cell analysis later on. Optimized tandems reach 78% of their radiative V_{OC} limit, see Figure 3c and maximum power point (MPP) tracking, displayed in the inset of Figure 3b, shows that the optimized all-perovskite tandems reach PCE's of 23.4%, an improvement of ≈2.5% absolute compared to the control tandems.

In order to optimize the efficiency of the tandems further, we then implemented the three previously optimized high-gap perovskite compositions. The bandgap shift from 1.80 to 1.85 eV and 1.88 eV can be well seen in external quantum efficiency (EQE) spectra in all-perovskite tandems made thereof (**Figure 4**a). Naturally, the three different high-gap subcells also influence the absorption onset of the LG perovskite. Using different bandgaps allowed us to improve the current matching between the HG and LG subcells, which is crucial for a monolithic tandem interconnection (see Figure S3, Supporting Information for integrated EQE values and Figure S20, Supporting Information for the current mismatch between HG and LG subcell).

As shown in Figure 4b, the V_{OC} of fabricated all-perovskite tandems increases with increasing HG-perovskite bandgap, and best performing all-perovskite tandems based on a 1.85 eV HG-perovskite reach 23.7% according to MPP tracking with a champion V_{OC} of 2.00 V. The forward and reverse JV of this champion device can be found in Figure S5, Supporting Information.

Interestingly, the J_{SC} of our 1.80/1.27 eV tandem combination exhibits a relatively high J_{SC} equal to the integrated EQE from the HG subcell, although this tandem combination should be limited by the LG subcell producing a somewhat lower integrated EQE current. We performed all measurements with an illumination mask and confirmed that the spectral mismatch between our sun simulator and AM 1.5G is very small (see Figure S19, Supporting Information) to exclude potential overestimations and thereby confirm that the J_{SC} measured from *JV* is correct and not overestimated. Device statistics, displayed in Figure S4, Supporting Information, further corroborate that our tandems—especially the 1.8/1.27 eV HG/LG combination – can operate without strict current matching. We believe this is caused by a rather low shunt resistance within the LG subcell, and show electrical simulations and sub-cell selective resistive photovoltage measurements highlighting the existence and the impact of low shunt resistances in the LG subcell on tandem solar cell operation and performance in the SI (see Note S1, Supporting Information as well as Figures S17 and S18, Supporting Information). Importantly, Figure S18, Supporting Information, also shows that while the observed shunts in the LG cell can lift the current matching condition, the shunts will still reduce the PCE due to a concurrent reduction in FF, thus not causing an overestimation of the PCE. Indeed, looking at a statistical analysis of our fabricated devices we observe that the 1.80/1.27 eV tandem combination exhibits a larger J_{SC} but lower FF in comparison to the better current matched 1.85/1.27 eV and 1.88/1.27 eV combinations (see Figure S4, Supporting Information).

2.4. Sub-Cell Analysis

In order to get a deeper insight into the factors limiting the performance of these optimized tandem solar cells, we performed more detailed sub-cell selective EL measurements. Hereby we apply a forward bias to the tandem device that injects a current into both subcells. EL within both subcells then can be measured in the dark and easily distinguished by their

© 2022 The Authors. Advanced Energy Materials published by Wiley-VCH GmbH

corresponding photon energy, for example, around 1.80, 1.85, and 1.88 eV for the HG-Perovskite subcells and 1.27 eV for the LG-subcell respectively, see also EL spectra displayed in Figure S6, Supporting Information. In order to measure the EL quantum yield (ELQY) as a function of injection current, we used appropriate long-pass and short-pass filters together with a large-area Silicon-photodiode. Analogous to the PL, we can calculate the $QFLS_{EL}$ from the measured ELQY for each injection current J_{inj} using Equation (2).

$$QFLS_{EL} = k_B T \cdot \ln\left(ELQY \cdot \frac{J_{inj}}{J_{0,rad}}\right) \quad (2)$$

Radiative dark current $J_{0,rad}$ values were calculated from EQE measurements, as detailed in the experimental methods, and we summarize results in Figures S7 and S8, Supporting Information, as well as Table S1, Supporting Information for the different perovskites. Plotting the implied or pseudo-voltage ($_{ps}V_{EL} = QFLS_{EL}/e$) on the x–axis and the J_{inj} current minus J_{SC} ($J = J_{inj} - J_{SC}$) on the y–axis allows us to derive pseudo-light-JV curves from the measured ELQY values. The derived pseudo-JV-characteristics are not only free of parasitic transport losses but most importantly reveal pseudo-JV-characteristics of the individual subcells, which cannot be accessed using standard JV measurements under illumination. We show EL-pseudo-JV curves of the individual subcells for all-perovskite tandems based on the 1.85/1.27 eV bandgap combination in **Figure 5**a alongside the summarized pseudo-JV curves representing the resulting tandem as well as standard JV characteristics under AM1.5G. Open and closed symbols refer to control and threefold optimized HG subcells that we prepared within

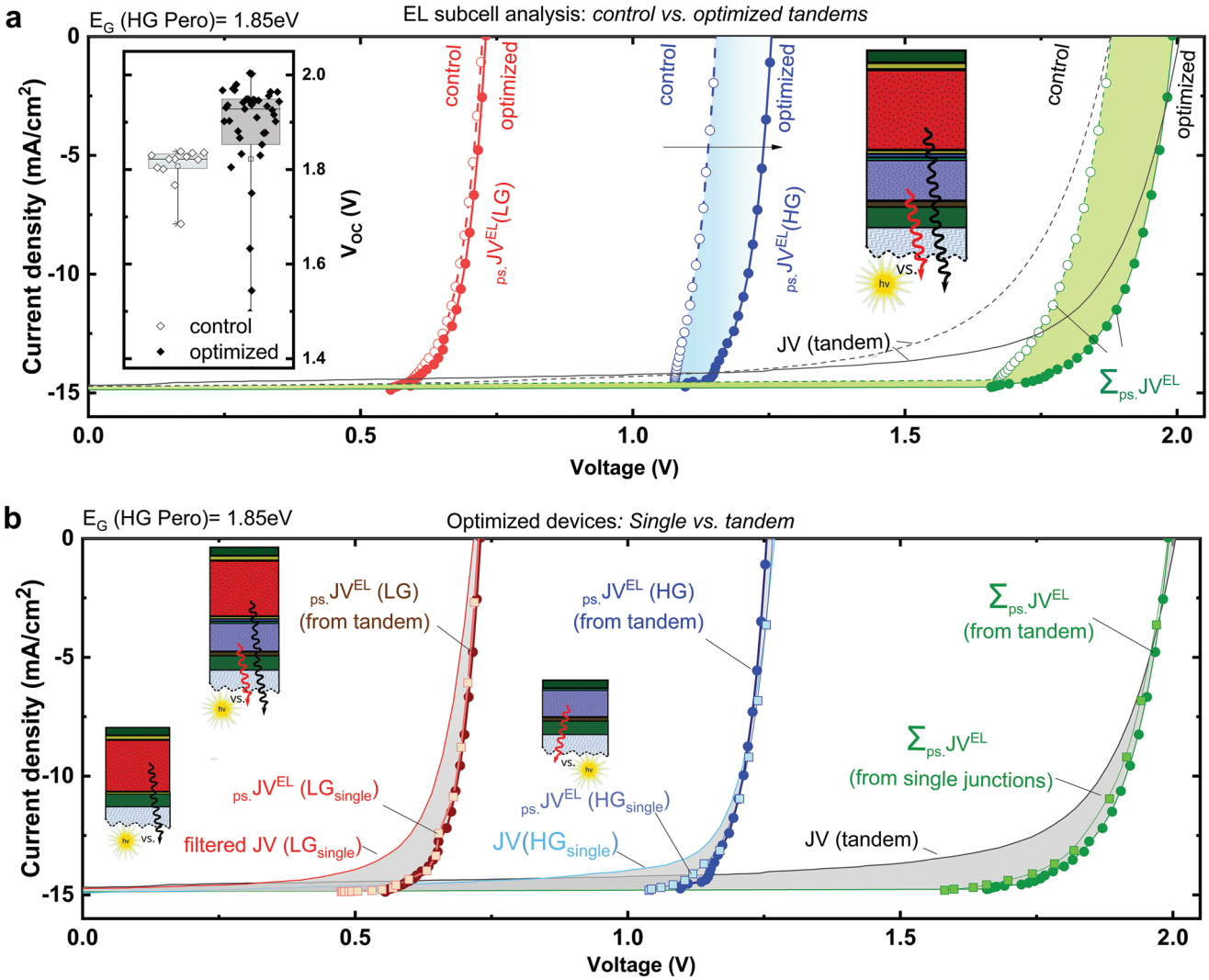

Figure 5. a) Pseudo JV curves from EL for an optimized and control tandem based on a 1.85 eV HG $Cs_{0.05}(FA_{0.55}MA_{0.45})_{0.95}Pb(I_{0.55}Br_{0.45})_3$ perovskite. Shown are the individual subcell pseudo-JV curves as well as the resulting (added) tandem pseudo-JV curves in comparison with traditional JV curves measured under AM1.5G. The inset displays V_{OC}s obtained from the JV curves of optimized and control tandems employing a 1.85 eV HG perovskite. b) Comparison between pseudo-JV curves obtained from an optimized 1.85/1.27 eV tandem and pseudo-JV curves obtained from single junctions based on the same perovskites. Corresponding JV curves for both single junction and tandem devices are plotted alongside to highlight FF losses.

© 2022 The Authors. Advanced Energy Materials published by Wiley-VCH GmbH

the same batch to avoid batch-to-batch variations. Comparison of the subcell pseudo-*JV*'s clearly shows that the improvement in the tandem V_{OC} of $\Delta V_{OC}^{tandem} \approx 120$ mV between control and optimized devices, directly results from the optimized HG subcell featuring an improvement of 120 mV. Both values are corroborated by the mean V_{OC} improvement of 0.10 V we observe when evaluating statistics as shown as inset in Figure 5a.

To analyze this V_{OC} improvement further, we compare in Figure 5b pseudo-*JV* characteristics of the optimized tandem (closed circles) to the corresponding EL-pseudo-*JV* characteristics of identically prepared single junctions (open square symbols). Notably, the LG perovskite pseudo-*JV*s in the tandem and in the single junction are identical, indicating that there are no V_{OC} losses stemming from the integration in the tandem device. The optimized HG perovskite shows a slight (≈20 mV) decrease in V_{OC} upon incorporation in a tandem device. This could be caused by the processing of the LG perovskite on top of the HG subcell, but the difference is so small it could also be the result of device-to-device variation. On the other hand, the pseudo-FFs (psFF) and pseudo-PCEs (psPCE) of the HG subcell are improved in the tandem compared to psFF and psPCE of identically prepared HG single junctions. Our interconnect—comprising an ultrathin layer of indium oxide and a layer of tin oxide, both deposited by atomic layer deposition on top of a spin coated layer of Al doped ZnO nanoparticles previously only applied in perovskite/organic tandems[41]—therefore can be considered quasi lossless.

Finally, we compare in Figure 5b, the pseudo-*JV*s (symbols) to regular *JV* curves for HG and LG single junctions (lines) measured under AM1.5 and HG-filtered AM1.5G, respectively. It can be seen here that the V_{OC} and pseudo-V_{OC} ($_{ps}V_{OC}$) match very well. The FFs on the other hand are much lower than their corresponding pseudo-FFs, especially for the LG perovskite. This indicates that the cells suffer from severe transport losses, while the EL pseudo-JV measurements are only sensitive to the total non-radiative recombination losses analogously to a dark-*JV* curve and barely affected by resistive losses.[45] Overall, we can conclude that the FF can be improved from 74.6% to 84.6% by optimizing the charge transport in both subcells, which could enable an efficiency of 25.2%. (**Table 2**)

We further note that when using EL, a measurement that is performed in dark, care has to be taken on transient effects that are barely present under full AM1.5G illumination. Especially for the LG perovskite, the ELQY can increase upon light soaking of the cell as well as upon keeping the cell biased at V_{OC} in the dark. We show examples of this effect in Figures S6 and S9, Supporting Information as well as the impact on extracted pseudo-*JV* characteristics from EL measurements in Figure S10, Supporting Information. Pseudo-JV characteristics we analyzed here were taken after the cell reached a steady-state comparable to standard *JV* measurements under AM1.5G. We note that the derived $_{ps}V_{OC}$ at $J_{inj.} = J_{gen}$ conditions must equal the device V_{OC} if Rau´s reciprocity is fulfilled.[46] This is generally observed for perovskite cells,[47,48] and therefore a good sanity check of the EL and derived pseudo-*JV* characteristics. If done properly, injection-dependent ELQY measurements reveal accurate pseudo-light *JV* characteristics that allow us to obtain a comprehensive overview of the limiting factors.

Finally, we also perform intensity-dependent PL measurements on the optimized tandems, and compare the results to those from ELQY. **Figure 6**a displays the QFLS as a function of the equivalent injected current (ELQY) or generated current density (PLQY). If plotted on a semi-logarithmic scale the data follows a linear slope given by the subcell/tandem ideality factor. And while the ideality factors are relatively similar we notice significantly higher QFLS for PLQY measurements compared to ELQY for both the LG and the HG subcells. The discrepancy between these two values indicates energy level offsets present in the device stack, causing a difference between QFLS generated under illumination (i.e., from PLQY) and the device V_{OC}. Note that the QFLS from EL equals the device V_{OC} if Rau's reciprocity is fulfilled.[46] In Figure S11, Supporting Information, simulated energy diagrams alongside a simulated *JV* curve corroborate the impact of potential energy level offsets. We note that the discrepancies between QFLS determined by EL and PL are also present in our single junction devices (see Figure S12, Supporting Information), and thus stem from energy level offsets already present in the single junction stacks, rather than energy level offsets introduced by incorporation in the tandem cell or the recombination layer. Reducing such energy level offsets would enable us to minimize the QFLS discrepancy between ELQY and PLQY results, and push the efficiencies up further toward the potential indicated by the PLQY measurements at 27.0% versus 25.2% from ELQY. Corresponding intensity-dependent PL measurements, as well as a comparison between pseudo-*JV*s obtained from EL and PL measurements can be found in Figures S13 and S14, Supporting Information, respectively.

Looking beyond the transport losses and QFLS–V_{OC} mismatch, we ultimately also investigate the efficiency potential of the isolated absorber materials through intensity-dependent PLQY measurements. Figure 6b displays pseudo *JV* curves from ELQY and PLQY measurements on the tandems, alongside the pseudo-*JV* characteristics from PLQY measurements on the isolated perovskite layers, and clearly shows the limitations imposed by the transport layers. The combination of our 1.27 eV LG perovskite with the 1.85 eV HG perovskite reaches an absorber efficiency potential of 28.4% with an implied V_{OC} of 2.22 V. Notably our threefold optimized 1.85/1.27 eV HG/LG champion tandem with a V_{OC} of 2.00 V already reaches 84% of this material potential. Although we have now optimized the

Table 2. Summary of implied V_{OC} and efficiency potentials from EL for optimized 1.85/1.27 eV HG/LG based perovskite tandems, compared to device parameters measured under AM1.5G. Note that the comparison presented here was made on one exemplary device, while we summarize further device parameters and statistics in Figure S3, Supporting Information. J_{SC} in all cases was equal to J_{gen} of 14.87 mA.

		$_{ps}V_{OC}$ [V]	$_{ps}$FF [%]	$_{ps}$PCE [%]
HG subcell	From EL	1.26	88.2	16.4
LG subcell	From EL	0.73	80.6	8.8
Tandem	From EL	1.99	84.6	25.2
Tandem	AM1.5	2.00	74.6	21.4
HG single junction	From EL	1.27	84.3	15.9
HG single junction	AM1.5	1.27	78.7	15.6
LG single junction	From EL	0.73	81.3	8.8
LG single junction	HG filtered AM1.5	0.72	71.2	7.6

© 2022 The Authors. Advanced Energy Materials published by Wiley-VCH GmbH

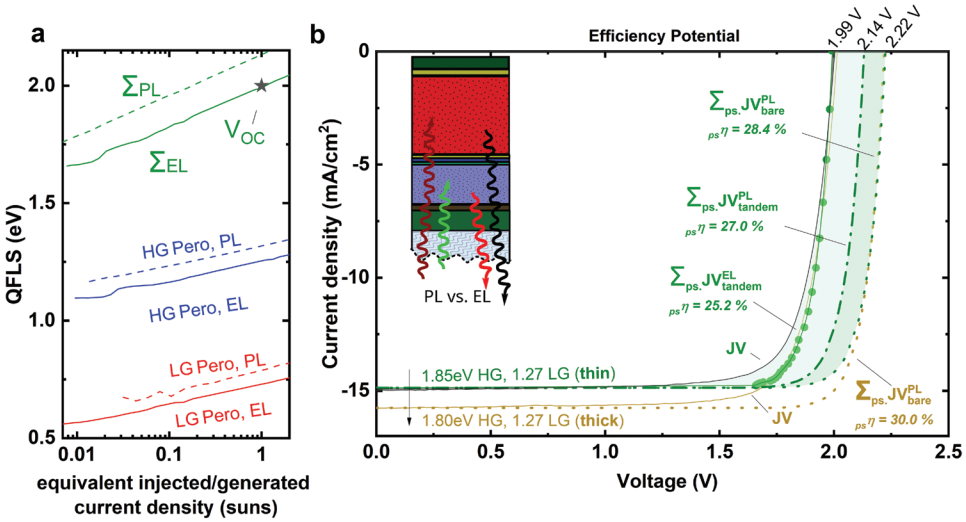

Figure 6. a) QFLS of the HG and LG perovskite subcells in a 1.85 eV/1.27 eV tandem calculated from ELQY or PLQY as a function of the equivalent injected current density (ELQY) or generated current density (PLQY) respectively. Summed QFLS representing the actual tandem are further shown alongside the V_{OC} obtained from *JV* characteristics under AM1.5G b) Pseudo-*JV*s reconstructed from EL (solid line) and PL (dashed line) tandem measurements, displayed alongside a pseudo-*JV* reconstructed from a PL measurement of isolated perovskite layers. The latter indicates the material efficiency potential. Displayed for tandems based on a standard thin (green) LG absorber with and an optimized thick (golden) LG absorber, with improved current density.

device V_{OC} by focusing on improving the HG perovskite, we note that the tandems still suffer from a limited short circuit current due to the lead-tin perovskite not being thick enough to absorb all the light. Therefore, as an ultimate optimization step, we increase the thickness of the LG perovskite, using a fabrication method adapted from Hu et al.[49] thereby reaching higher EQE values at long wavelengths (see Figure S15, Supporting Information for EQE). In combination with our optimized 1.80 eV HG subcells this increases the tandem current and ultimately boosts the device efficiency to 25.2% (JV) and 25.9% stabilized (MPP tracking in Figure S16, Supporting Information). With this increased tandem current, the material potential determined from isolated absorber layers reaches 30.0%, as can be seen in Figure 6b, thereby exemplifying the enormous potential of this PV technology.

3. Conclusion

In this work, we identified V_{OC} losses in all-perovskite tandem solar cells and show that in our present material set, as well as many literature devices, nonradiative recombination within the high-bandgap perovskite subcell dominates V_{OC} and performance losses. We developed a multifaceted optimization route to improve the high-bandgap subcell by replacing the HTL PTAA by 2PACz, adding oleylamine to the perovskite in combination with including a thin LiF layer between the perovskite and the ETL. In an additive manner, our combined approach enables high-gap perovskite absorbers with high QFLS and an improved V_{OC} potential, reaching 83% of their radiative V_{OC} limit. The high V_{OC} potential translated directly to the V_{OC} of the all-perovskite tandems that were subsequently fabricated, and improved their steady-state power conversion efficiency to 23.7% for our champion combination of 1.85/1.27 eV HG/LG perovskite subcells. We performed a thorough subcell analysis to disentangle further factors limiting the performance of these tandem devices and found that although there is still room for improvement of the V_{OC}s of both individual subcells, our ultrathin InO_x based interconnect is quasi lossless, and both subcells reach V_{OC}s equally high to those in their respective single junctions. The FF on the other hand is significantly lower than the pseudo-FF obtained from EL measurements, indicating significant transport losses. Reducing such transport losses would allow us to approach efficiencies of 25.2%, which is the efficiency potential for our 1.85/1.27 eV HG/LG perovskite tandem combination extracted from EL-based pseudo-*JV* characteristics. We also observe a discrepancy between the pseudo-V_{OC} obtained from EL measurements, and the QFLS obtained from PLQY measurements, the latter being significantly higher. This indicates there are energy barriers present in the stack, which, when reduced, will provide a significant additional optimization potential, enabling efficiencies of up to 27.0%. Concluding, the indium oxide interconnect that was used in these tandems is quasi lossless, but both individual subcells, specifically the low-gap after the optimization of the high-gap perovskite, can still be improved to reach better performances, as we demonstrate with a proof-of-concept device which, due to a thicker LG absorber, reaches 25.9% stabilized efficiency, with an ultimate efficiency potential of 30%. The insights of this extensive subcell-selective characterization provide crucial feedback and allow us to develop evidence-based optimization routes to improve the tandem efficiencies further in the future.

Supporting Information

Supporting Information is available from the Wiley Online Library or from the author.

© 2022 The Authors. Advanced Energy Materials published by Wiley-VCH GmbH

Acknowledgements

The authors would like to thank Thomas Kirchartz for insightful discussions and feedback. This work was part-funded by EPSRC, project number EP/S004947/1. The authors acknowledge funding from the Deutsche Forschungsgemeinschaft (DFG, German Research Foundation) within the SPP 2196 (HIPSTER 424709669 and SURPRISE 423749265). The authors further acknowledge financial support by the Federal Ministry for Economic Affairs and Energy within the framework of the 7th Energy Research Programme (P3T-HOPE, 03EE1017C) and HyPerCells (a joint graduate school of the Potsdam University and the Helmholtz Zentrum Berlin). J.T. thanks the Rank Prize fund for financial support. M.S. acknowledges the Heisenberg program from the Deutsche Forschungsgemeinschaft (DFG, German Research Foundation) for funding—project number 498155101. K.B. and T.R. thank the DFG (HIPSTER PRO:RI 1551/15-2), the BMBF (MOISTURE: 01DP20008 and the EU Horizon 2020 (FOXES: 951774) for funding. F.L. acknowledges funding from the Volkswagen Foundation via the Freigeist Program.

Open access funding enabled and organized by Projekt DEAL.

Conflict of Interest

H.J.S. is co-founder and CSO of Oxford PV Ltd.

Author Contributions

J.T. contributed to conceptualization, formal analysis, investigation, visualization, and writing—original draft; F.P.-C. contributed to conceptualization, formal analysis, investigation, and visualization; K.O.B. contributed to investigation, formal analysis, visualization, and writing—review and editing; E.G.-P. contributed to investigation; F.Y. contributed to investigation and writing—review and editing; J.W. contributed to writing—review and editing; S.A. contributed to funding acquisition, resources, and supervision; T.R. contributed to funding acquisition, resources, writing—review and editing, and supervision; D.N. contributed to funding acquisition, resources, writing—review and editing, and supervision; H.J.S. contributed to funding acquisition, writing—review and editing, and supervision; M.S. contributed to conceptualization, funding acquisition, writing—review and editing, and supervision; F.L. contributed to conceptualization, formal analysis, investigation, visualization, writing–original draft, and supervision.

Data Availability Statement

The data that support the findings of this study are available from the corresponding author upon reasonable request.

Keywords

all-perovskite tandem, efficiency potential, photovoltaics, recombination losses, subcell-selective diagnosis

Received: August 5, 2022
Revised: November 5, 2022
Published online:

[1] F. Hao, C. C. Stoumpos, R. P. H. Chang, M. G. Kanatzidis, *J. Am. Chem. Soc.* **2014**, *136*, 8094.
[2] Z. Yang, A. Rajagopal, C. C. Chueh, S. B. Jo, B. Liu, T. Zhao, A. K. Y. Jen, *Adv. Mater.* **2016**, *28*, 8990.
[3] G. E. Eperon, T. Leijtens, K. A. Bush, R. Prasanna, T. Green, J. T. W. Wang, D. P. McMeekin, G. Volonakis, R. L. Milot, R. May, A. Palmstrom, D. J. Slotcavage, R. A. Belisle, J. B. Patel, E. S. Parrott, R. J. Sutton, W. Ma, F. Moghadam, B. Conings, A. Babayigit, H. G. Boyen, S. Bent, F. Giustino, L. M. Herz, M. B. Johnston, M. D. McGehee, H. J. Snaith, *Science* **2016**, *354*, 861.
[4] A. Rajagopal, Z. Yang, S. B. Jo, I. L. Braly, P. W. Liang, H. W. Hillhouse, A. K. Y. Jen, *Adv. Mater.* **2017**, *29*, 1702140.
[5] D. Zhao, Y. Yu, C. Wang, W. Liao, N. Shrestha, C. R. Grice, A. J. Cimaroli, L. Guan, R. J. Ellingson, K. Zhu, X. Zhao, R. G. Xiong, Y. Yan, *Nat. Energy* **2017**, *2*, 17018.
[6] T. Todorov, T. Gershon, O. Gunawan, Y. S. Lee, C. Sturdevant, L. Y. Chang, S. Guha, *Adv. Energy Mater.* **2015**, *5*, 1500799.
[7] C. D. Bailie, M. G. Christoforo, J. P. Mailoa, A. R. Bowring, E. L. Unger, W. H. Nguyen, J. Burschka, N. Pellet, J. Z. Lee, M. Grätzel, R. Noufi, T. Buonassisi, A. Salleo, M. D. McGehee, *Energy Environ. Sci.* **2015**, *8*, 956.
[8] F. Lang, M. A. Gluba, S. Albrecht, J. Rappich, L. Korte, B. Rech, N. H. Nickel, *J. Phys. Chem. Lett.* **2015**, *6*, 2745.
[9] S. Albrecht, M. Saliba, J. P. Correa Baena, F. Lang, L. Kegelmann, M. Mews, L. Steier, A. Abate, J. Rappich, L. Korte, R. Schlatmann, M. K. Nazeeruddin, A. Hagfeldt, M. Grätzel, B. Rech, *Energy Environ. Sci.* **2016**, *9*, 81.
[10] J. P. Mailoa, C. D. Bailie, E. C. Johlin, E. T. Hoke, A. J. Akey, W. H. Nguyen, M. D. McGehee, T. Buonassisi, *Appl. Phys. Lett.* **2015**, *106*, 121105.
[11] F. Lang, G. E. Eperon, K. Frohna, E. M. Tennyson, A. Al-Ashouri, G. Kourkafas, J. Bundesmann, A. Denker, K. G. West, L. C. Hirst, H. C. Neitzert, S. D. Stranks, *Adv. Energy Mater.* **2021**, *11*, 2102246.
[12] D. N. Weiss, *Joule* **2021**, *5*, 2247.
[13] R. Lin, K. Xiao, Z. Qin, Q. Han, C. Zhang, M. Wei, M. I. Saidaminov, Y. Gao, J. Xu, M. Xiao, A. Li, J. Zhu, E. H. Sargent, H. Tan, *Nat. Energy* **2019**, *4*, 864.
[14] R. Lin, J. Xu, M. Wei, Y. Wang, Z. Qin, Z. Liu, J. Wu, K. Xiao, B. Chen, S. Min Park, G. Chen, H. R. Atapattu, K. R. Graham, J. Xu, J. Zhu, L. Li, C. Zhang, E. H. Sargent, H. Tan, *Nature* **2022**, *603*, 73.
[15] Z. Yang, Z. Yu, H. Wei, X. Xiao, Z. Ni, B. Chen, Y. Deng, S. N. Habisreutinger, X. Chen, K. Wang, J. Zhao, P. N. Rudd, J. J. Berry, M. C. Beard, J. Huang, *Nat. Commun.* **2019**, *10*, 4498.
[16] K. Xiao, R. Lin, Q. Han, Y. Hou, Z. Qin, H. T. Nguyen, J. Wen, M. Wei, V. Yeddu, M. I. Saidaminov, Y. Gao, X. Luo, Y. Wang, H. Gao, C. Zhang, J. Xu, J. Zhu, E. H. Sargent, H. Tan, *Nat. Energy* **2020**, *5*, 870.
[17] T. Leijtens, R. Prasanna, K. A. Bush, G. E. Eperon, J. A. Raiford, A. Gold-Parker, E. J. Wolf, S. A. Swifter, C. C. Boyd, H. P. Wang, M. F. Toney, S. F. Bent, M. D. McGehee, *Sustainable Energy Fuels* **2018**, *2*, 2450.
[18] E. T. Hoke, D. J. Slotcavage, E. R. Dohner, A. R. Bowring, H. I. Karunadasa, M. D. McGehee, *Chem. Sci.* **2015**, *6*, 613.
[19] F. Penã-Camargo, P. Caprioglio, F. Zu, E. Gutierrez-Partida, C. M. Wolff, K. Brinkmann, S. Albrecht, T. Riedl, N. Koch, D. Neher, M. Stolterfoht, *ACS Energy Lett.* **2020**, *5*, 2728.
[20] T. J. Jacobsson, A. Hultqvist, A. García-Fernández, A. Anand, A. Al-Ashouri, A. Hagfeldt, A. Crovetto, A. Abate, A. G. Ricciardulli, A. Vijayan, A. Kulkarni, A. Y. Anderson, B. P. Darwich, B. Yang, B. L. Coles, C. A. R. Perini, C. Rehermann, D. Ramirez, D. Fairen-Jimenez, D. di Girolamo, D. Jia, E. Avila, E. J. Juarez-Perez, F. Baumann, F. Mathies, G. S. A. González, G. Boschloo, G. Nasti, G. Paramasivam, G. Martínez-Denegri, et al., *Nat. Energy* **2022**, *7*, 107.
[21] T. Kirchartz, U. Rau, M. Hermle, A. W. Bett, A. Helbig, J. H. Werner, *Appl. Phys. Lett.* **2008**, *92*, 123502.

© 2022 The Authors. Advanced Energy Materials published by Wiley-VCH GmbH

[22] S. Roensch, R. Hoheisel, F. Dimroth, A. W. Bett, *Appl. Phys. Lett.* **2011**, *98*, 251113.
[23] S. Chen, L. Zhu, M. Yoshita, T. Mochizuki, C. Kim, H. Akiyama, M. Imaizumi, Y. Kanemitsu, *Sci. Rep.* **2015**, *5*, 7836.
[24] D. Alonso-Álvarez, N. Ekins-Daukes, *IEEE J. Photovoltaics* **2016**, *6*, 1004.
[25] F. Lang, E. Köhnen, J. Warby, K. Xu, M. Grischek, P. Wagner, D. Neher, L. Korte, S. Albrecht, M. Stolterfoht, *ACS Energy Lett.* **2021**, *6*, 3982.
[26] R. Sheng, M. T. Hörantner, Z. Wang, Y. Jiang, W. Zhang, A. Agosti, S. Huang, X. Hao, A. Ho-Baillie, M. Green, H. J. Snaith, *J. Phys. Chem. C* **2017**, *121*, 27256.
[27] D. Zhao, C. Chen, C. Wang, M. M. Junda, Z. Song, C. R. Grice, Y. Yu, C. Li, B. Subedi, N. J. Podraza, X. Zhao, G. Fang, R. G. Xiong, K. Zhu, Y. Yan, *Nat. Energy* **2018**, *3*, 1093.
[28] A. F. Palmstrom, G. E. Eperon, T. Leijtens, R. Prasanna, S. N. Habisreutinger, W. Nemeth, E. A. Gaulding, S. P. Dunfield, M. Reese, S. Nanayakkara, T. Moot, J. Werner, J. Liu, B. To, S. T. Christensen, M. D. McGehee, M. F. A. M. van Hest, J. M. Luther, J. J. Berry, D. T. Moore, *Joule* **2019**, *3*, 2193.
[29] J. Tong, Z. Song, D. H. Kim, X. Chen, C. Chen, A. F. Palmstrom, P. F. Ndione, M. O. Reese, S. P. Dunfield, O. G. Reid, J. Liu, F. Zhang, S. P. Harvey, Z. Li, S. T. Christensen, G. Teeter, D. Zhao, M. M. Al-Jassim, M. F. A. M. van Hest, M. C. Beard, S. E. Shaheen, J. J. Berry, Y. Yan, K. Zhu, *Science* **2019**, *364*, 475.
[30] Z. Yu, Z. Yang, Z. Ni, Y. Shao, B. Chen, Y. Lin, H. Wei, Z. J. Yu, Z. Holman, J. Huang, *Nat. Energy* **2020**, *5*, 657.
[31] H. Gao, Q. Lu, K. Xiao, Q. Han, R. Lin, Z. Liu, H. Li, L. Li, X. Luo, Y. Gao, Y. Wang, J. Wen, Z. Zou, Y. Zhou, H. Tan, *Sol. RRL* **2021**, *5*, 2100814.
[32] K. Datta, J. Wang, D. Zhang, V. Zardetto, W. H. M. Remmerswaal, C. H. L. Weijtens, M. M. Wienk, R. A. J. Janssen, *Adv. Mater.* **2022**, *34*, 2110053.
[33] A. Al-Ashouri, A. Magomedov, M. Roß, M. Jošt, M. Talaikis, G. Chistiakova, T. Bertram, J. A. Márquez, E. Köhnen, E. Kasparavičius, S. Levcenco, L. Gil-Escrig, C. J. Hages, R. Schlatmann, B. Rech, T. Malinauskas, T. Unold, C. A. Kaufmann, L. Korte, G. Niaura, V. Getautis, S. Albrecht, *Energy Environ. Sci.* **2019**, *12*, 3356.
[34] J. Dagar, M. Fenske, A. Al-Ashouri, C. Schultz, B. Li, H. Köbler, R. Munir, G. Parmasivam, J. Li, I. Levine, A. Merdasa, L. Kegelmann, H. Näsström, J. A. Marquez, T. Unold, D. M. Többens, R. Schlatmann, B. Stegemann, A. Abate, S. Albrecht, E. Unger, *ACS Appl. Mater. Interfaces* **2021**, *13*, 13022.
[35] J. Seo, S. Park, Y. C. Kim, N. J. Jeon, J. H. Noh, S. C. Yoon, S. il Seok, *Energy Environ. Sci.* **2014**, *7*, 2642.
[36] M. Stolterfoht, C. M. Wolff, J. A. Márquez, S. Zhang, C. J. Hages, D. Rothhardt, S. Albrecht, P. L. Burn, P. Meredith, T. Unold, D. Neher, *Nat. Energy* **2018**, *3*, 847.
[37] X. Zheng, Y. Hou, C. Bao, J. Yin, F. Yuan, Z. Huang, K. Song, J. Liu, J. Troughton, N. Gasparini, C. Zhou, Y. Lin, D. J. Xue, B. Chen, A. K. Johnston, N. Wei, M. N. Hedhili, M. Wei, A. Y. Alsalloum, P. Maity, B. Turedi, C. Yang, D. Baran, T. D. Anthopoulos, Y. Han, Z. H. Lu, O. F. Mohammed, F. Gao, E. H. Sargent, O. M. Bakr, *Nat. Energy* **2020**, *5*, 131.
[38] E. L. Unger, L. Kegelmann, K. Suchan, D. Sörell, L. Korte, S. Albrecht, *J. Mater. Chem. A* **2017**, *5*, 11401.
[39] S. Mahesh, J. M. Ball, R. D. J. Oliver, D. P. McMeekin, P. K. Nayak, M. B. Johnston, H. J. Snaith, *Energy Environ. Sci.* **2020**, *13*, 258.
[40] Z. Liu, J. Siekmann, B. Klingebiel, U. Rau, T. Kirchartz, *Adv. Energy Mater.* **2021**, *11*, 2003386.
[41] K. O. Brinkmann, T. Becker, F. Zimmermann, C. Kreusel, T. Gahlmann, M. Theisen, T. Haeger, S. Olthof, C. Tückmantel, M. Günster, T. Maschwitz, F. Göbelsmann, C. Koch, D. Hertel, P. Caprioglio, F. Peña-Camargo, L. Perdigón-Toro, A. Al-Ashouri, L. Merten, A. Hinderhofer, L. Gomell, S. Zhang, F. Schreiber, S. Albrecht, K. Meerholz, D. Neher, M. Stolterfoht, T. Riedl, *Nature* **2022**, *604*, 280.
[42] K. O. Brinkmann, J. Zhao, N. Pourdavoud, T. Becker, T. Hu, S. Olthof, K. Meerholz, L. Hoffmann, T. Gahlmann, R. Heiderhoff, M. F. Oszajca, N. A. Luechinger, D. Rogalla, Y. Chen, B. Cheng, T. Riedl, *Nat. Commun.* **2017**, *8*, 13938.
[43] T. Gahlmann, K. O. Brinkmann, T. Becker, C. Tückmantel, C. Kreusel, F. van gen Hassend, S. Weber, T. Riedl, *Adv. Energy Mater.* **2020**, *10*, 1903897.
[44] K. O. Brinkmann, T. Becker, F. Zimmermann, C. Kreusel, T. Gahlmann, T. Haeger, T. Riedl, *Sol. RRL* **2021**, *5*, 2100371.
[45] M. Stolterfoht, M. Grischek, P. Caprioglio, C. M. Wolff, E. Gutierrez-Partida, F. Peña-Camargo, D. Rothhardt, S. Zhang, M. Raoufi, J. Wolansky, M. Abdi-Jalebi, S. D. Stranks, S. Albrecht, T. Kirchartz, D. Neher, *Adv. Mater.* **2020**, *32*, 2000080.
[46] U. Rau, *Phys. Rev. B: Condens. Matter Mater. Phys.* **2007**, *76*, 085303.
[47] K. Tvingstedt, O. Malinkiewicz, A. Baumann, C. Deibel, H. J. Snaith, V. Dyakonov, H. J. Bolink, *Sci. Rep.* **2014**, *4*, 6071.
[48] M. Stolterfoht, P. Caprioglio, C. M. Wolff, J. A. Márquez, J. Nordmann, S. Zhang, D. Rothhardt, U. Hörmann, Y. Amir, A. Redinger, L. Kegelmann, F. Zu, S. Albrecht, N. Koch, T. Kirchartz, M. Saliba, T. Unold, D. Neher, *Energy Environ. Sci.* **2019**, *12*, 2778.
[49] S. Hu, K. Otsuka, R. Murdey, T. Nakamura, M. A. Truong, T. Yamada, T. Handa, K. Matsuda, K. Nakano, A. Sato, K. Marumoto, K. Tajima, Y. Kanemitsu, A. Wakamiya, *Energy Environ. Sci.* **2022**, *15*, 2096.

© 2022 The Authors. Advanced Energy Materials published by Wiley-VCH GmbH